Tellus
SERIES A
DYNAMIC
METEOROLOGY
AND OCEANOGRAPHY
PUBLISHED BY THE INTERNATIONAL METEOROLOGICAL INSTITUTE IN STOCKHOLM

Tellus (2011), 63A, 1038–1051

TELLUS

On the use of Finite-Time Lyapunov Exponents and Vectors for direct assimilation of tracer images into ocean models

By OLIVIER TITAUD[1,2]*, JEAN-MICHEL BRANKART[1] and JACQUES VERRON[1], [1]*LEGI, CNRS & Université de Grenoble, BP53X, 38041 Grenoble Cedex, France;* [2]*CERFACS, 42 avenue Gaspard Coriolis, 31057 Toulouse, Cedex 01, France*

(Manuscript received 31 January 2011; in final form 21 June 2011)

ABSTRACT

Satellite ocean tracer images, of sea surface temperature (SST) and ocean colour images, for example, show patterns like fronts and filaments that characterize the flow dynamics. These patterns can be described using Lagrangian tools such as Finite-Time Lyapunov Exponents (FTLE) or Finite-Time Lyapunov Vectors (FTLV). In recent years, several studies have investigated the possibility of directly assimilating structured data from satellite images into numerical models. In this paper, we exploit specific properties of FTLE and FTLV to define observation operators that can be used in a direct ocean tracer image assimilation scheme. In an idealized context, we show that high-resolution SST and ocean colour images can be exploited to correct velocity fields using FTLE or FTLV.

1. Introduction

Data Assimilation techniques combine all the available information to perform a 'realistic' simulation of a dynamic system. This information comes from different sources: mathematical models based on physical laws, observations and a priori knowledge (e.g. errors). The techniques are widely used to simulate geophysical fluid flows. They may be based on sequential filtering (Carme et al., 2001; Brasseur and Verron, 2006) or variational (Le Dimet and Talagrand, 1986; Luong et al., 1998) approaches. Both involve an objective function that evaluates the discrepancy between model outputs and observations using a least-squares term. This term takes the following general form:

$$J(X) = \|\mathcal{H}(X) - \mathbf{y}\|^2_{\mathcal{O}}, \tag{1}$$

where $X \in \mathcal{X}$ and $\mathbf{y} \in \mathcal{O}$ are, respectively, the state variable and the observation vectors. Assimilation schemes are designed to minimize the objective function with respect to the state (or control) variable X.

The difference is evaluated in the observation space $\mathcal{O}$ using the norm $\|\cdot\|_{\mathcal{O}}$: the so-called *observation operator* $\mathcal{H}$ maps the state variable space $\mathcal{X}$ onto the observation space. The norm is usually derived from an inner product that takes into account the observation error statistics (e.g. measurement and representativity errors). When observed variables correspond to certain state variables, $\mathcal{H}$ may 'simply' represent a projection in space and time. This is generally the case of in situ observations like temperature or salinity profiles in the oceanographic context. Remote observations from infrared or colour radiometers installed on satellites are radiances that are indirectly linked to the state variables. The corresponding observation operator may then contain complex radiative transfer laws. Another way of assimilating this kind of data is to invert radiance measurements into pseudo-observations of a state variable. Typical examples are the infrared and microwaves radiances that are inverted, respectively, into surface temperature and salinity measurements. However, the link between radiance measurements and the concentration of bio-geochemical tracers (such as chlorophyll) is far more complex. Assimilation of these radiances is still the subject of intensive research (see e.g. Carmillet et al., 2001; Gregg, 2008).

The improvement of remote sensing systems has resulted in to satellite images of increasing resolution that show mesoscale and submesoscale patterns such as filaments, fronts and eddies (see Fig. 1). The location, shape and evolution of these structures are strongly linked to flow dynamics (Ottino, 1989). A single ocean tracer image integrates the past temporal evolution of the velocity field that advected it (Lehahn et al., 2007); also, as with passive tracer gradients in a turbulent flow, ocean tracer gradients become aligned in certain specific orientations

*Corresponding author.
e-mail: contact@oliviertitaud.fr
DOI: 10.1111/j.1600-0870.2011.00533.x

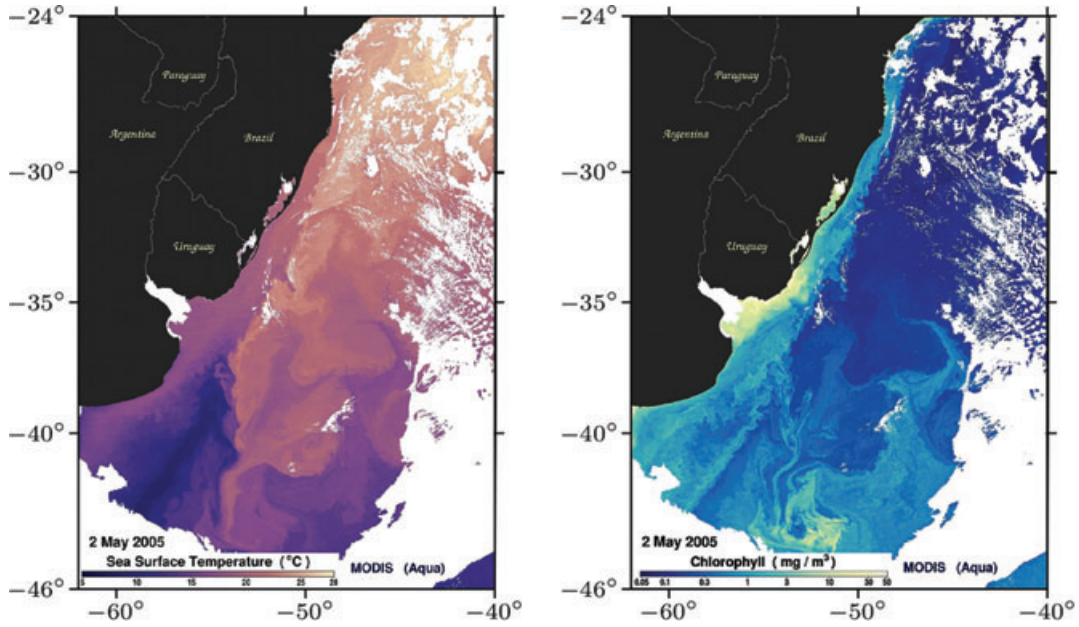

Fig. 1. Sea surface temperature (left panel) and ocean colour (right panel) images from the products of AQUA MODIS remote instrument showing structured patterns such as fronts and filaments off the coast of Argentina. Convergence of the southward flowing Brazil and northward flowing Malvinas currents, 2 May 2005. Courtesy: NASA.

(namely the orientation of backward Finite-Time Lyapunov Vectors (FTLV), see Section 3) which in turn characterize the velocity field (Lapeyre, 2002). However, structured information contained in ocean tracer images are still underused by forecasting systems. Recent work has been conducted to develop methodologies for assimilating such data into numerical models, and today two different approaches are under study. The first (which is not examined in this paper) assimilates pseudo-observations of velocity fields produced from image sequences using the motion estimation technique (Horn and Schunck, 1981; Herlin et al., 2004). This approach takes into account little physical information about the underlying processes that are observed in the image. The second approach, referred to as Direct Image Assimilation (DIA) in this paper, *directly* assimilates the image data into the dynamic model: in Corpetti et al. (2009) the image pixel is assimilated as a tracer concentration measurement; in Titaud et al. (2010) the structured information extracted from the image are assimilated using an adapted observation operator. The latter does not use the pixel basis of the image but higher levels of interpretation (e.g. a multiscale decomposition or a description of contours). It requires observation operators that link the structured information from the image with the model output.

In this paper we adopt the second approach and show the relevance of using Finite-Time Lyapunov Exponents (FTLE, Pierrehumbert and Yang, 1993) in the DIA framework. FTLE is a Lagrangian tool that was introduced to characterize coherent structures in time-dependent flows. Together with Finite-Size Lyapunov Exponents (FSLE, Artale et al., 1997; Aurell et al., 1997) FTLEs are widely used in oceanography to link ocean tracer distribution with mesoscale geostrophic currents in order to study stirring and mixing processes (Abraham and Bowen, 2002; d'Ovidio et al., 2004; Lehahn et al., 2007). The main objective of our paper is to show, in an idealized, experimental, but fairly realistic test case, that *high-resolution* ocean tracer images may be exploited to correct *larger scale* velocity fields using a DIA framework. We suggest using sophisticated observation operators based on the computation of FTLE and FTLV. Their construction does not require the numerical advection of a synthetic passive tracer, as was the case in Titaud et al. (2010).

The paper is organized as follows: in Section 2 we briefly describe the test case used in our experiments. In Section 3 we review the definitions of FTLE and FTLV (FTLE-V) associated with a time-dependent flow, and point out the properties that are relevant to this work. The use of this Lagrangian tool in a DIA framework is described in Section 4. In Section 5 we detail the methodology of our study and then present and discuss the main results. The conclusions of the study are presented in Section 6.

2. Test case

Our study is based on a 1-yr simulation of an idealized biophysical model of a subregion of the North Atlantic Ocean. The coupled model (Krémeur et al., 2009, described in) is applied to a double-gyre configuration that mimics the North Atlantic Ocean circulation and its western boundary current system. A $1/54^{\circ}$ high-resolution version of this configuration (referred as R54 in this paper) has been carried out by Lévy et al. (2009,

2010). It is of interest here because it emphasizes in particular the importance of submesoscale dynamics. The physical component of the model is based on the NEMO-OPA code which is quite a standard ocean global circulation model based on primitive equations (Madec, 2008). The biogeochemical component comes from the NEMO-TOP2 passive tracer engine based on the rather simple six-compartment LOBSTER model (Lévy et al., 2001). The vertical resolution of the model is non-uniform, with 5 m at the top and 250 m at the bottom. We are particularly interested in the respective dynamical and biogeochemical tracers such as temperature and phytoplankton. As we are concerned with the application of satellite images, we focus on the *surface activity*.

The 'reference domain' Ω of our study is a $6^\circ \times 6^\circ$ square subdomain of the full double-gyre configuration. This domain is located between longitudes -74.62°E and -68.62°E and latitudes 22.36°N and 28.36°N:

$$\Omega = [-74.62, -68.62] \times [22.36, 28.36]. \quad (2)$$

This region is located in the southeast recirculation branch of the—idealized—Gulf Stream (see Fig. 2, left-hand panel: Ω is marked by a dashed box). It is characterized by strong eddy activity associated with fairly active submesoscale patterns. It is typical of the strong turbulent activity associated with the mid-latitude non-linear and unstable jets of the world ocean. We arbitrarily choose day $k_0 = 99$ to be the *reference date* which corresponds to 9 April. Sea surface temperature (SST) and Mixed Layer Phytoplankton (MLP) fields show the main characteristic patterns that can be found in ocean tracer fields (see Fig. 4): a mesoscale eddy is located on the northeast side of the domain, and a front on the east side; submesoscale filaments are also observed. The results presented in this paper are independent of the reference date and the subdomain Ω: other experiments with other reference dates and subdomains have resulted in the same conclusions (not shown). Note that MLP is closely linked with ocean colour image products.

3. FTLE and FTLV

3.1. Definition

The transport of a tracer in a fluid is closely related to emergent patterns that are commonly referred to as *coherent structures*. For time-independent dynamic systems, they correspond to stable and unstable manifolds of hyperbolic trajectories (Wiggins, 1992). Coherent structures delimit regions of whirls, stretching or contraction of tracer (Ottino, 1989): contraction is observed along stable manifolds whereas unstable manifolds correspond to divergent directions along which the tracer is stretched. Stable and unstable manifolds are *material curves* that act as transport barriers : they cannot be crossed by fluid particles. Generalizing these concepts to flows with general time dependence is not straightforward and is still the subject of an intense research. Studies that concern theoretical and practical aspects of coherent structures deal with their rigorous definition and their detection. When coherent structures are defined using fluid trajectories they are often called Lagrangian Coherent Structures (LCS). Haller and Yuan (2000) define an LCS as a material curve (more precisely a material surface in an extended phase space) which exhibits locally the strongest attraction, repulsion or shearing in the flow over a finite-time interval. A rigorous mathematical theory that fits with this physical concept was recently developed in Haller (2011) where quantitative and robust criteria are given to identify hyperbolic (i.e. repelling and attracting) LCSs. However, and despite some caveats detailed in Haller (2011), LCSs are usually identified in a practical

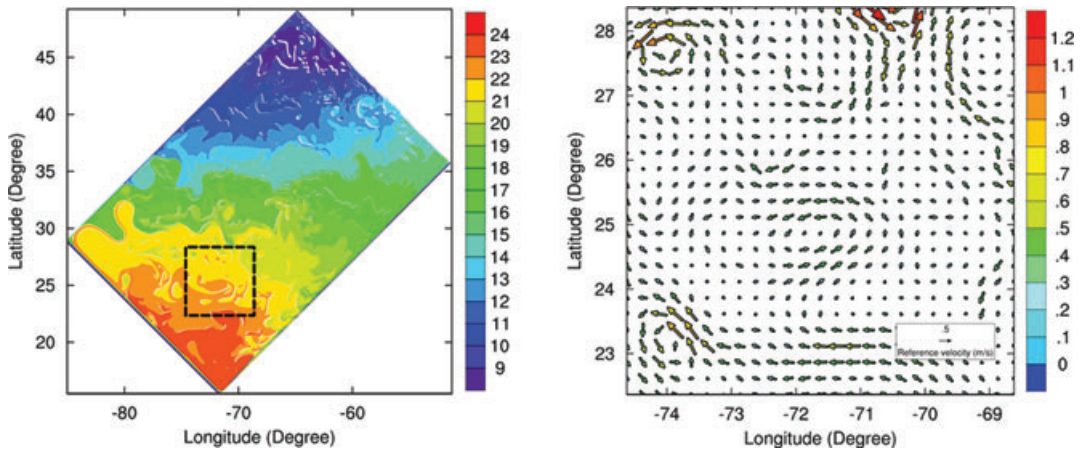

Fig. 2. Left panel: SST (°C) field of an idealized simulation of the North Atlantic Ocean using the $1/54^\circ$ horizontal resolution model of Lévy et al. (2009, 2010). Our study region is contained in the dashed box. Right panel: surface model mesoscale velocity field (m s^{-1}) filtered from this simulation in the domain and at the reference date of our study.

manner as maximizing ridges of FTLE field (Haller, 2001a,b, 2002; Shadden et al., 2005; Mathur et al., 2007). FTLE are defined as the largest eigenvalue of the Cauchy–Green strain tensor of the flow map (see later for more details). The corresponding eigenvector is called FTLV in this paper. FTLE and the *orientation* of FTLV constitute the key tools used in this work. FTLEs are widely used to characterize transport processes in oceanographic flows where the velocity field is only known as a *finite data set* (Lekien et al., 2005; Beron-Vera et al., 2008; Olascoaga et al., 2008; Beron-Vera and Olascoaga, 2009; Shadden et al., 2009; Beron-Vera et al., 2010; Olascoaga, 2010). Even if not used in this paper we also mention the FSLE (Aurell et al., 1997; Artale et al., 1997), which is another Lagrangian tool that is commonly used in oceanographic contexts for studying mixing processes (d'Ovidio et al. 2004; Lehahn et al. 2007; d'Ovidio et al. 2009a,b, and references therein). We refer to Peacock and Dabiri (2010) who review the use of FTLE for detecting LCSs in other contexts.

Here, we briefly review the definitions of FTLE and FTLV before pointing out certain properties that we exploit in this paper. FTLE is a scalar local notion that represents the rate of separation of initially neighbouring particles over a finite-time window $[t_0,\ t_0 + T]$, $T \neq 0$. Let $\mathbf{x}(t) = \mathbf{x}(t;\ \mathbf{x}_0,\ t_0)$ be the position of a Lagrangian particle at time t, started at $\mathbf{x}_0$ at $t = t_0$ and advected by the time-dependent fluid flow $\mathbf{u}(\mathbf{x}, t)$, $\mathbf{x} \in \Omega$, $t \in [t_0, t_0 + T]$. Thus we have

$$\begin{cases} \dfrac{D\mathbf{x}(t)}{Dt} = \mathbf{u}(\mathbf{x}(t), t), \\ \mathbf{x}(t_0) = \mathbf{x}_0. \end{cases} \tag{3}$$

An infinitesimal perturbation $\delta\mathbf{x}(t)$ started at $t = t_0$ from $\delta_0 = \delta\mathbf{x}(t_0)$ around $\mathbf{x}_0$ then verifies, for all $t \in [t_0, t_0 + T]$,

$$\begin{cases} \dfrac{D\delta\mathbf{x}(t)}{Dt} = \nabla\mathbf{u}(\mathbf{x}(t), t).\delta\mathbf{x}(t), \\ \delta\mathbf{x}(t_0) = \delta_0, \quad \mathbf{x}(t_0) = \mathbf{x}_0. \end{cases} \tag{4}$$

The Forward Finite-Time Lyapunov Exponent at a point $\mathbf{x}_0 \in \Omega$ and for an advection time T is defined as the growth factor of the norm of the perturbation $\delta\mathbf{x}_0$ started around $\mathbf{x}_0$ and advected by the flow after the finite advection time T. Maximal stretching occurs when $\delta\mathbf{x}_0$ is aligned with the eigenvector associated with the maximum eigenvalue $\lambda_{\max}$ of the Cauchy-Green strain tensor:

$$\Delta = \left[\nabla\phi_{t_0}^{t_0+T}(\mathbf{x}_0)\right]^* \left[\nabla\phi_{t_0}^{t_0+T}(\mathbf{x}_0)\right]. \tag{5}$$

The flow map of the system (3) $\phi_{t_0}^{t} : \mathbf{x}_0 \mapsto \mathbf{x}(t; \mathbf{x}_0, t_0)$ links the location $\mathbf{x}_0$ of a Lagrangian particle at $t = t_0$ to its position $\mathbf{x}(t;\ \mathbf{x}_0,\ t_0)$ at time $t \neq t_0$. This eigenvector is referred to as the *forward* FTLV and we denote it by $\varphi_{t_0}^{t_0+T}(\mathbf{x}_0)$. We thus have

$$\max_{\delta\mathbf{x}_0} \|\delta\mathbf{x}(T)\| = \sqrt{\lambda_{\max}(\Delta)}\|\overline{\delta\mathbf{x}_0}\|, \tag{6}$$

where $\overline{\delta\mathbf{x}_0}$ is aligned with $\varphi_{t_0}^{t_0+T}(\mathbf{x}_0)$. Finally, the *forward* FTLE at the point $\mathbf{x}_0 \in \Omega$ and for an advection time T starting at $t = t_0$ is defined as

$$\sigma_{t_0}^{t_0+T}(\mathbf{x}_0) = \frac{1}{|T|} \ln \sqrt{\lambda_{\max}(\Delta)}. \tag{7}$$

We are particularly interested in backward FTLE field whose ridges approximate attracting LCSs (Haller, 2011). *Backward* FTLE-Vs are similarly defined, with the time direction being inverted in (3). For more details on the practical computation of FTLE-V, see for example, Shadden et al. (2005, 2009) and Ott (1993) for any types of flows and d'Ovidio et al. (2004) for oceanic flows.

As previously mentioned, FTLE (FTLV) is a scalar (vector) that is computed at a given location $\mathbf{x}_0$. Seeding a domain with particules initially located on a grid leads to the computation of a discretized scalar (FTLE) and vector (FTLV) fields. Our study focuses on the sensibility of the distribution of FLTE-V *over the test case domain* Ω with respect to small perturbations of the *time-dependent* flow $\mathbf{u}$ along a *fixed* time period $[t_0,\ t_0 + T]$. Consistently with this variational approach, we will later consider the operators $\Sigma[\mathbf{u}] : \mathbf{x} \in \Omega \to \sigma_{t_0}^{t_0+T}(\mathbf{x}) \in \mathbb{R}$ and $\Phi[\mathbf{u}] : \mathbf{x} \in \Omega \to \varphi_{t_0}^{t_0+T}(\mathbf{x}) \in \mathbb{R}^2$. These operators map the flow $\mathbf{u}$ with the FTLE-V distribution over Ω. The dependence of this map to the window $[t_0, t_0 + T]$ is not studied in this paper: it is fixed in our experiments as it should be in an operational context (see Section 5.1.1). We then chose not to mention this dependence explicitly in order to simplify notations. Shadden et al. (2005) discuss the dependence of FTLE to the time advection T and its consequence on the properties of LCS marked by FTLE ridges.

An example of backward FTLE and corresponding backward FTLV orientation maps, computed from a mesoscale time-dependent velocity field, is given in Fig. 3.

3.2. Connection between FTLE-V and tracers fields

In this paper we exploit two properties of backward FTLE-V to construct adapted observation operators for direct ocean tracer image assimilation (Titaud et al., 2010).

The first property concerns the contours of FTLE maps. Backward FTLE fields show contours that correspond reasonably well to the main structures such as filaments, fronts and spirals that appear in geophysical and bio-geochemical tracer fields (Beron-Vera et al., 2010; Shadden et al., 2009; Olascoaga et al., 2008, 2006). Figure 3 (left panel) shows a backward FTLE field (7) in the reference domain and at the reference date of our study. This field is computed from a sequence of *mesoscale* (1/4°) time-dependent velocity fields filtered from the R54 test case simulation (see Section 5.1.1 for more details of the computation settings for our experiments). The main geometrical patterns of this field are clearly visible in the corresponding SST and MLP fields of the R54 simulation (i.e. same reference domain and date): see Fig. 4. In this study, we adopt the direct image assimilation approach described in Titaud et al. (2010): first, we

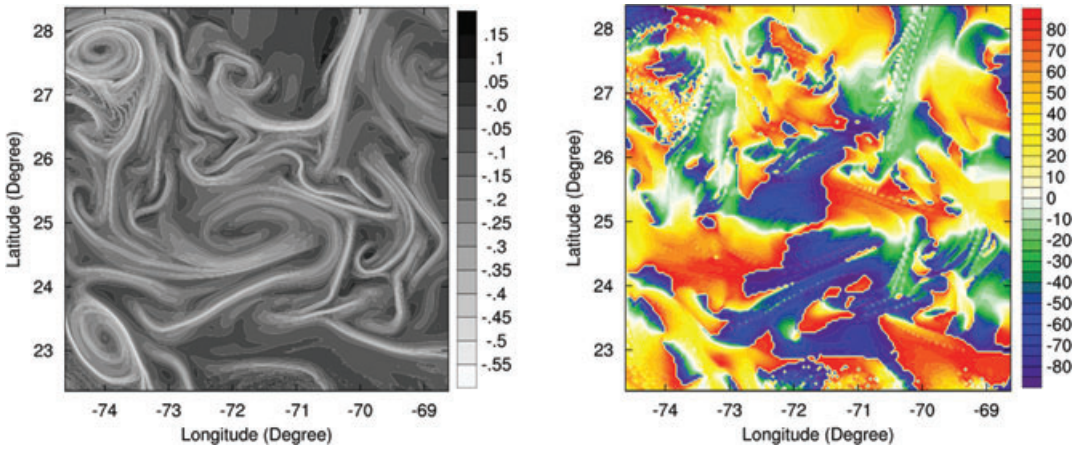

Fig. 3. Backward FTLE (day^{-1}) (left) and corresponding backward FTLV orientations (angular degree) (right) computed in the reference domain and at the reference date of our study. These fields are computed from a *mesoscale* (1/4°) time-dependent velocity fields sequence filtered from the R54 test case simulation.

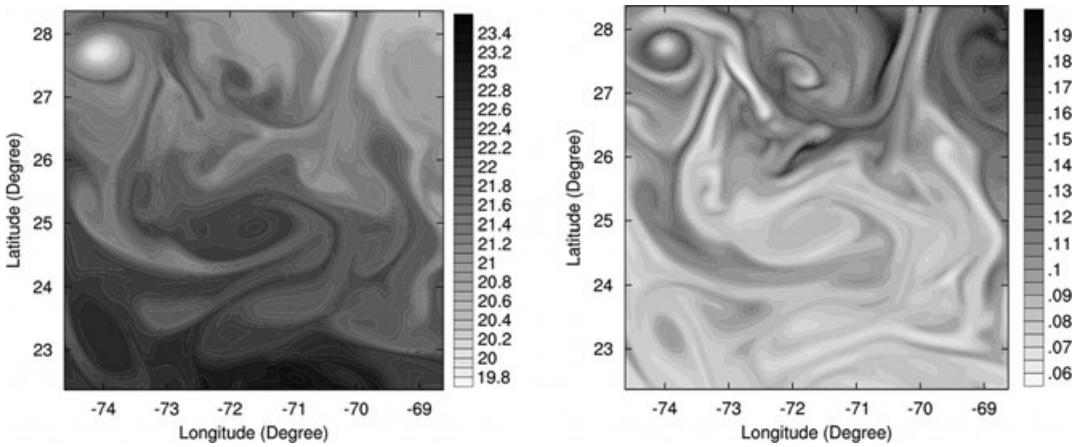

Fig. 4. SST (°C) (left) and MLP concentration (mmole-N m^{-3}) (right) fields of the R54 test case simulation in the reference domain and at the reference date of our study. These tracer fields show pronounced typical patterns such as an eddy (North East corner), a front (East side) and filaments.

will consider FTLE field as it were a tracer field which in turn can be considered as an image. This makes sense because of the almost-Lagrangian nature of FTLE (Shadden et al., 2005):

$$\mathrm{d}\sigma_{t_0}^{t_0+T}(\mathbf{x}_0)/\mathrm{d}t_0 = O(1/|T|). \tag{8}$$

Second, we are *exclusively* interested in the location and shape of the structures that appear in the FTLE and tracer fields: we do not exploit the *value* (pixel intensity) of the exponents or the concentration.

The second property concerns the orientations of FTLVs. Lapeyre (2002) shows that for a freely decaying 2D turbulence flow, the orientation of the gradient of a *passive* tracer converges to that of backward FTLVs. This dynamic behaviour of the tracer concentration gradient ∇q is explained by the fact that $\mathbf{k} \times \nabla q$ verifies the same eq. (4) as $\delta\mathbf{x}$ does ($\mathbf{k}$ being the unit vertical vector). Such alignment properties have also been observed for realistic oceanic flows and tracers (d'Ovidio et al., 2009b). Figure 5 shows the dynamic alignment of SST and MLP gradients with FLTV: the root mean square (RMS) angular error between backward FTLV orientations computed at a given date and tracer gradient field orientations decreases with time. Figure 3 (right panel) shows the orientations of the backward FTLV that correspond to the aforementioned FTLE field (left panel). In our idealized experiment, SST and MLP gradients also show similar orientations: see Fig. 6.

These two properties (pattern matching between tracer and FTLE scalar fields and tracer gradient orientation alignment with FTLV orientation) are the first interesting properties that can be exploited in a DIA framework. Furthermore, Beron-Vera et al. (2010) and Beron-Vera (2010) showed, using real data, that these properties remain valid with a mesoscale advection, that is, when the resolution of the velocity field—from which FTLE-V are computed—is much lower than the resolution of the observed tracer field. This behaviour was also mentioned using another

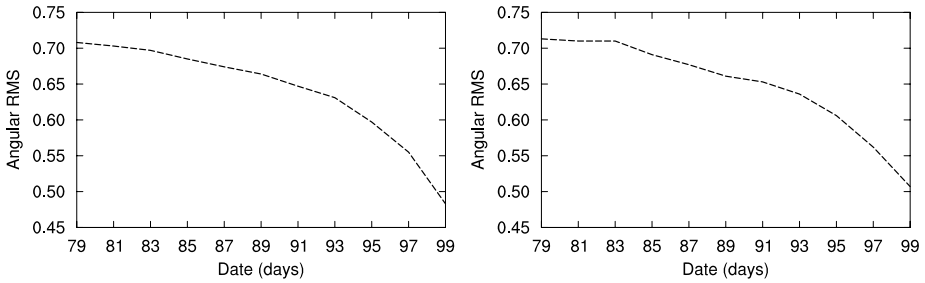

Fig. 5. Dynamic alignment of SST (left) and MLP (right) gradient orientations with FTLV orientations: in both cases, angular RMS between tracer gradient and FTLV orientations computed at the reference date 99 decreases with time.

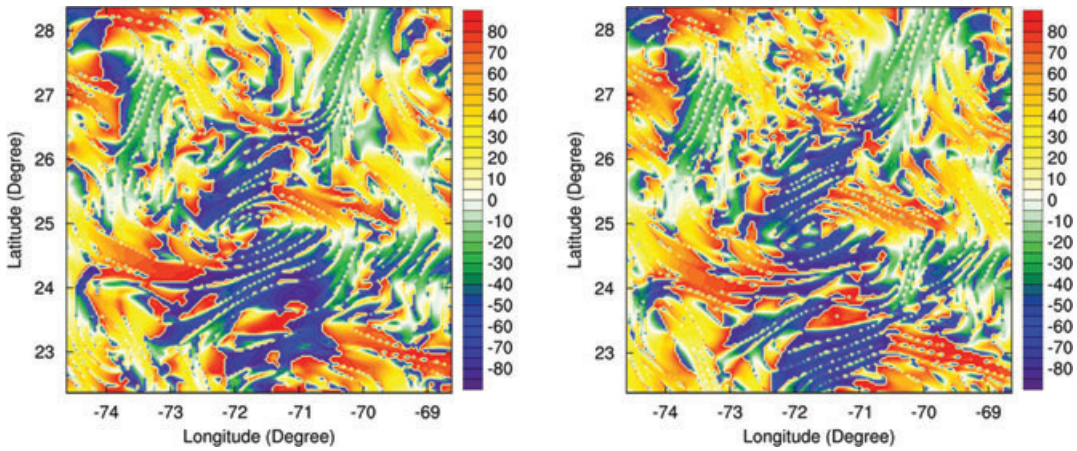

Fig. 6. Orientations (angular degree) of the gradients of the SST (left) and MLP (right) fields shown in Fig 4.

Lagrangian tool (FSLE) by Lehahn et al. (2007) and d'Ovidio et al. (2009b). Our synthetic data exhibit the same behaviour: FTLE field of Fig. 3 is computed from a mesoscale $1/4^\circ$ velocity field on the same high-resolution ($1/54^\circ$) grid as that used to compute the SST and MLP fields of Fig. 4. This feature is crucial from both a practical and physical point of view: first, velocity fields obtained from ocean global circulation models do not often provide more than mesoscale information, whereas tracer images contain submesoscale information; second, FTLE-V may be used to quantify and characterize the link between scales.

4. Direct image assimilation using FTLE-V

4.1. General framework

From a practical point of view, an image is an array of numbers known as pixels, but from a mathematical point of view it is more convenient to model an image as a bounded real valued function of two bounded continuous variables. This provides a powerful and rigorous framework with which to process or analyse them (Chan and Shen, 2005; Aubert and Kornprobst, 2006). In the following, in order to simplify our discussion, we employ the same notation for the discretized and the continuous version of the operators we respectively apply to the numerical and modelled image. In particular, the gradient operator ∇ is approximated by a first-order finite difference operator. In the following, $\mathcal{I}_\Xi$ denotes the set of discrete real positive valued functions defined on a rectangular grid $\Xi = [\![1, n]\!] \times [\![1, m]\!] \subset \mathbb{N}^2$ (more simply, $\mathcal{I}_\Xi$ is the set of $n \times m$ numerical images). The continuous version of $\mathcal{I}_\Xi$ is denoted by $\mathcal{I}$.

As in the case of human vision, the relevant information contained in an image is mainly provided by its discontinuities (Marr, 1982). This is why image assimilation focuses on the characterization of edges (or other structured information from the image) instead of the pixel values of the image. In our context, the pixel value of a satellite image (or more precisely a satellite product given in an image form) may correspond to the concentration of certain tracers. We emphasize that we are not interested in the assimilation of such measurements as in the classical cost function (1), but in the assimilation of the structured data that can be extracted from the image. With this in mind Titaud et al. (2010) suggest adding an *image* term to the classical cost function. This takes the general form

$$J_{\mathcal{S}}(X) = \|\mathcal{H}_{\mathcal{S}}(X) - \mathbf{y}^s\|^2_{\mathcal{S}}, \tag{9}$$

where $\mathbf{y}^s \in \mathcal{S}$ represents the structures extracted from the observed image $c \in \mathcal{I}$, $\|\cdot\|_{\mathcal{S}}$ is a measure of the discrepancy between the elements of $\mathcal{S}$, and $\mathcal{H}_{\mathcal{S}}$ is the corresponding *structure*

observation operator. It maps the state variable space $\mathcal{X}$ onto the observation space $\mathcal{S}$. $J_{\mathcal{S}}$ is the *DIA term associated with the triplet* $(\mathcal{H}_{\mathcal{S}}, \mathcal{S}, \|\cdot\|_{\mathcal{S}})$. In practice, $\mathbf{y}^s$ is obtained using a structure extraction operator S that acts on the actual observed image c: $\mathbf{y}^s = \mathrm{S}(c)$. This operator is not part of the assimilation procedure and may be defined using image analysis techniques.

In the following subsections, we define two DIA triplets $(\mathcal{H}_{\mathcal{S}}, \mathcal{S}, \|\cdot\|_{\mathcal{S}})$ that rely, respectively, on the aforementioned properties of FTLE and FTLV. In each case, we first define the structure space $\mathcal{S}$ and an appropriate discrepancy measure $\|\cdot\|_{\mathcal{S}}$. The structure extraction operator S is defined afterwards. We finish with the definition of the structure observation operator $\mathcal{H}_{\mathcal{S}}$. We show the relevance of these triplets in Section 5.

4.2. FTLE-based observation operator

We saw in Section 3.2 that FTLE fields exhibit similar contours to those in the corresponding ocean tracer fields. These contours mark the edges of the most relevant features in these images, such as filaments, fronts and eddies. This property (pattern matching) motivates the use of a space of contours $\mathcal{E}$ (which stands for "Exponent") to construct a DIA triplet $(\mathcal{H}_{\mathcal{E}}, \mathcal{E}, \|\cdot\|_{\mathcal{E}})$. This space is simply defined as the set of binarized images, that is, the subspace of $\mathcal{I}_{\Xi}$ whose elements take one of only two values (0 or 1):

$$\mathcal{E} = \{f : \Xi \to \{0, 1\}\}. \tag{10}$$

The distance between two elements f and g of $\mathcal{E}$ is given by the RMS norm

$$\|f - g\|_{\mathcal{E}} = \sqrt{\frac{1}{n \times m} \sum_{(i,j)\in\Xi} |f(i,j) - g(i,j)|^2}. \tag{11}$$

A basic technique for a rough extraction of edges from an image is based on the binarization of its gradient norm using a hard threshold. We define the structure extraction operator E applied to an image $c \in \mathcal{I}_{\Xi}$ by: for all $(i, j) \in \Xi$

$$\mathrm{E}(c)(i,j) = \begin{cases} 1 & \text{if} \quad \|\nabla c(i,j)\| > \epsilon, \\ 0 & \text{else,} \end{cases} \tag{12}$$

where $\epsilon > 0$ is a given threshold parameter. Structures extracted from the observed tracer image involved in (9) are then $\mathbf{y}^{\mathcal{E}} = \mathrm{E}(c)$ in this case. Once we have defined the structure space and its associated discrepancy measure between two elements, we need to define the corresponding observation operator $\mathcal{H}_{\mathcal{E}}$ that maps the state variable space $\mathcal{X}$ onto the observation space $\mathcal{E}$. In this case, we are interested in comparing the contours in the tracer and the backward FTLE fields (7) at a reference date t_0. We then define the observation operator as the binarization of the backward FTLE gradient norm field, computed from the modelled time-dependent velocity field $\mathbf{u}$, at the reference date t_0:

$$\mathcal{H}_{\mathcal{E}}(X) = \mathrm{E}(\Sigma[\mathbf{u}]), \tag{13}$$

where the backward FTLE is viewed as an image operator acting on the flow field onto the image space $\mathcal{I}$:

$$\begin{aligned} \Sigma[\mathbf{u}] : \Omega &\to \mathbb{R} \\ \mathbf{x} &\mapsto \sigma_{t_0}^{t_0+T}(\mathbf{x}). \end{aligned} \tag{14}$$

Finally, the FTLE-based DIA cost function (9) associated with the triplet $(\mathcal{H}_{\mathcal{E}}, \mathcal{E}, \|\cdot\|_{\mathcal{E}})$ is written as

$$J_{\mathcal{E}}(\mathbf{u}) = \|\mathrm{E}_{\epsilon'}\big(\Sigma[\mathbf{u}]\big) - \mathrm{E}_{\epsilon}(c)\|_{\mathcal{E}}^2, \tag{15}$$

in which we make the dependence of E on ϵ in (12) explicit, because it does not necessarily take the same value for the tracers and the FTLE fields.

Technical details on the computation of the FTLE fields and the choice of the threshold parameter ϵ are given in Section 5.1.1 The edge extraction technique (12) together with distance (11) can be used to obtain a rough comparison of the location of fronts and patches on two images. Though more sophisticated image contour extraction techniques exist (see review of Chan and Shen, 2005), the results obtained with this basic method are nevertheless promising. Figure 7 shows the corresponding binarisation of the gradient of SST, MLP and backward FTLE fields presented in Figs 4 and 3, respectively. We can clearly see the relatively good match between the binarized FTLE and tracer gradient fields.

4.3. FTLV-based observation operator

In Section 3.2 we noticed that the orientations of the gradients of an ocean tracer image (or concentration field) are almost aligned with the backward FTLV orientations of the corresponding flow where the tracer is advected. This property motivates the use of backward FTLV as a tool for building an observation operator that links the velocity field of an ocean model to ocean tracer images. We will construct the corresponding FTLV-based DIA triplet in the same way as we constructed the FTLE-based DIA triplet $(\mathcal{H}_{\mathcal{E}}, \mathcal{E}, \|\cdot\|_{\mathcal{E}})$ in the previous section, starting with the definition of the structure space: as we want to compare the orientations of tracer image gradients with the FTLV orientations, we define the structure space $\mathcal{V}$ (which stands for "Vector") as the space of functions on Ξ with values in S^2, the Euclidean unit sphere of $\mathbb{R}^2$:

$$\mathcal{V} = \{f : \Xi \to S^2\}. \tag{16}$$

The discrepancy between two elements f and g of $\mathcal{V}$ is defined by

$$\|f - g\|_{\mathcal{V}} = \sqrt{\frac{1}{n \times m} \sum_{i,j\in\Xi} \sin^2\left[\Theta\big(f(i,j)\big) - \Theta\big(g(i,j)\big)\right]}, \tag{17}$$

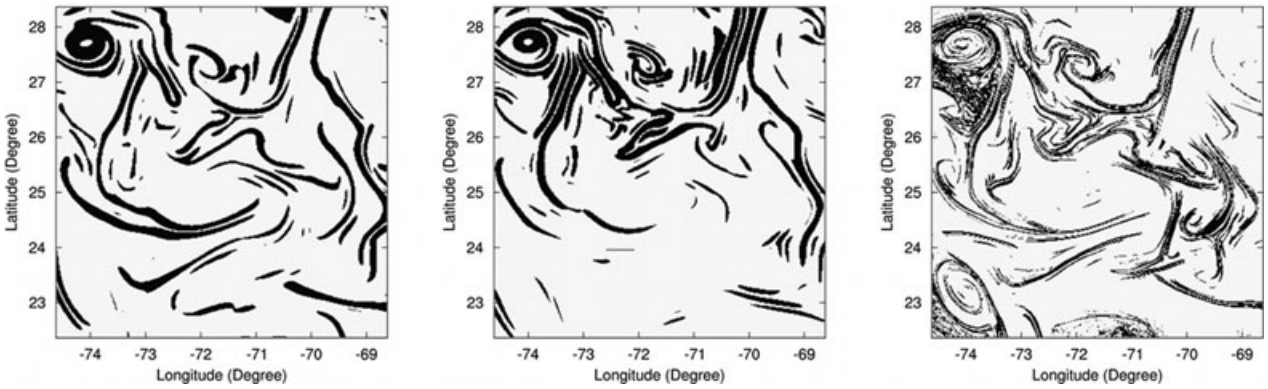

Fig. 7. Binarization of the SST (left), MLP (centre) and FTLE (right) gradient fields of Figs 4 and 3 using the threshold-based technique (12).

where $\Theta(\mathbf{w})$ represents the *orientation* of an element of $\mathbf{w} = (w_1, w_2) \in S^2$:

$$\Theta(\mathbf{w}) = \arctan(w_2/w_1) \in \left[-\frac{\pi}{2}, \frac{\pi}{2}\right]. \tag{18}$$

$\|f - g\|_{\mathcal{V}}$ measures the angular discrepancy between the straight lines whose normal directions are respectively f and g. We therefore emphasize that we are interested in comparing the *orientations* of two vectors, independently of their *directions*. We define the observed structures in the tracer image c as its normalized gradient field. We define for all $(i, j) \in \Xi$

$$\mathbf{y}^{\mathcal{V}}(i, j) = \mathrm{V}(c)(i, j) = \frac{\nabla c(i, j)}{\|\nabla c(i, j)\|} \in S^2. \tag{19}$$

As we want to compare the fields of tracer gradient orientations with the backward FTLV orientations, we define the observation operator as

$$\mathcal{H}_{\mathcal{V}}(X) = \Phi[\mathbf{u}], \tag{20}$$

where the backward FTLV field is computed at the reference date t_0. It is considered as an operator acting on the time-dependent flow field $\mathbf{u}$ onto $\mathcal{V}$:

$$\begin{array}{rccc} \Phi[\mathbf{u}] : & \Omega & \rightarrow & S^2 \\ & \mathbf{x} & \mapsto & \varphi_{t_0}^{t_0+T}(\mathbf{x}). \end{array} \tag{21}$$

Examples of FTLV orientation and tracer orientation fields are shown in Figs 3 (right panel) and 6, respectively. Finally, the FTLV-based DIA cost function (9) associated with the triplet $(\mathcal{H}_{\mathcal{V}}, \mathcal{V}, \|\cdot\|_{\mathcal{V}})$ is written as

$$J_{\mathcal{V}}(\mathbf{u}) = \|\Phi[\mathbf{u}] - \mathrm{V}(c)\|_{\mathcal{V}}^2. \tag{22}$$

5. Sensitivity studies

In this section, we experimentally show that backward FTLE-V can be used in a direct image assimilation framework to correct a *larger scale* velocity field from a *high-resolution* ocean tracer field showing submesoscale patterns.

5.1. Methodology

5.1.1. Computation settings. We want our framework to be close as possible to that of direct assimilation of high-resolution satellite images into *eddy-resolving* ocean models. In order to construct a consistent sequence of *mesoscale* velocity fields from the R54 simulation described in Section 2, we apply a space Lanczos filter to the *surface* model velocity field. The filter length is chosen so as to preserve mesoscale features. The result is interpolated on a $1/4^\circ$ horizontal resolution grid. We thus obtain a velocity sequence that represents a *mesoscale* view of the corresponding original *submesoscale* simulation. The mesoscale velocity field obtained can also be viewed as a mesoscale simulation with an ideally parametrized $1/54^\circ$ submesoscale physics. We should emphasize that the sequence of velocity fields $\mathbf{u}$ is only known as a finite-time data set: it represents a finite sequence of discrete velocity fields $(\mathbf{u}_k)_{k=k_0-T}^{k_0}$, k_0 being the reference date and T the advection time.

FTLE-V of the above sequence of filtered mesoscale velocity fields $(\mathbf{u}_k)_{k=k_0-T}^{k_0}$ are computed backward in time, from the reference date $k_0 = 99$, on the same $1/54^\circ$ horizontal resolution grid as the tracers fields. The backward advection of the particles is performed using a fourth-order Runge–Kutta scheme during a time period $T = 10$ days which corresponds to an eddy turnover time scale. The Cauchy–Green strain tensor (5) is approximated using a finite difference scheme. The initial separation parameter δ_0 in eq. (4) is chosen so that it is equal to the mesh size of the tracer grid, as suggested in d'Ovidio et al. (2004): $\delta_0 = 1/54^\circ$.

The threshold parameter ϵ involved in the definition of the structure extraction operator E in (12) is implicitly chosen such that a given percentage p of the values of the image gradient norm are larger than ϵ. This is a classical technique that allows p to be set regardless of the image c. In our experiments, we set $p = 0.8$.

5.1.2. Velocity perturbations modelling. A pre-requisite for a triplet $(\mathcal{H}, \mathcal{O}, \|\cdot\|_{\mathcal{O}})$ to be used to assimilate a data set $\mathbf{y} \in \mathcal{O}$ is that the corresponding cost function (1) has to be sensitive to perturbations of the state variable $X \in \mathcal{X}$. More specifically, we expect that the cost function admits a minimum value at the

non-perturbed state. In our experimental framework, we chose to study the behaviour of the cost function (9) with respect to the amplitude $\lambda \in \mathbb{R}$ of a perturbation δX. In other words, we are interested in the variation of the following sensitivity function

$$\lambda \in \mathbb{R} \mapsto \|\mathcal{H}_S(X + \lambda\delta X) - \mathbf{y}^S\|. \tag{23}$$

We expect it to be sufficiently smooth because standard descent-type minimization algorithms need such conditions to be efficient. Defining a set of perturbations is in general not a straightforward task and this is why we will consider a specific perturbation model. As this study is a preliminary step towards data assimilation, we construct a set of perturbations that is fairly consistent with the errors dealt with by such methods. We focus in particular on velocity errors because we want to show that structured information from ocean tracer images can be used to correct velocity fields.

Let $(\mathbf{u}_k)_{k=1,m+1}$ be the sequence of the one-year simulation mesoscale surface model velocity fields obtained from our test case, as described in the previous subsection. In this experiment, $m = 209$. We perform a principal components analysis using Empirical Orthogonal Functions (EOF) to decompose the signal, as used in Carme et al. (2001):

$$\mathbf{u}_k = \overline{\mathbf{u}} + \sum_{l=1}^{m} \alpha_k^{(l)} \mathbf{u}^{(l)}, \tag{24}$$

where $\overline{\mathbf{u}}$ is the time average velocity map. We define the climatological covariance matrix as follows:

$$\mathbf{P} = \frac{1}{m} \sum_{k=1}^{m+1} (\mathbf{u}_k - \overline{\mathbf{u}})(\mathbf{u}_k - \overline{\mathbf{u}})^*. \tag{25}$$

The EOFs $\mathbf{u}^{(l)}, l = 1, m$, are equal to the normalized eigenvectors of $\mathbf{P}$ times the square root of the corresponding eigenvalues. The time amplitudes $\alpha^{(l)}$ are normalized vectors. Figure 8 shows the inertia of the signal: the first EOF accounts for 10% of the total variance and 100 EOFs are required to account for 98% of total variance. Let $\mathbf{S}$ be the column matrix of the first $r = 100$ EOFs;

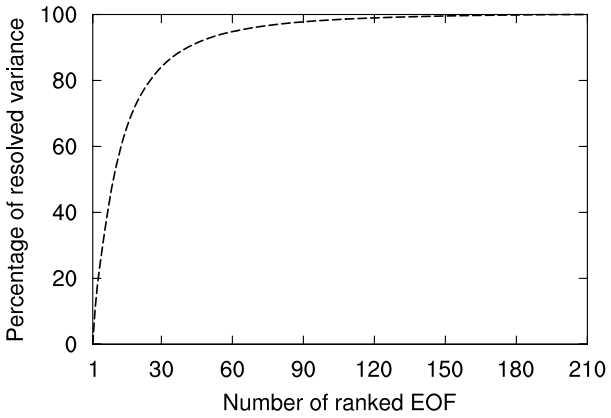

Fig. 8. Percentage of resolved variance as a function of the number of EOF.

$\mathbf{SS}^*$ represents the reduced rank square root representation of the covariance matrix $\mathbf{P}$. We consider the normally distributed velocity perturbations with zero mean and covariance $\mathbf{SS}^*$ of the sequence:

$$\delta\mathbf{u} \sim \mathcal{N}(0, \mathbf{SS}^*). \quad \delta\mathbf{u} = \sum_{l=1}^{r} \mathbf{u}^{(l)} \delta\gamma_l \quad \text{with} \quad \delta\gamma_l \sim \mathcal{N}(0, 1). \tag{26}$$

Assimilation schemes based on linear analysis (which are the most widely used and studied at the moment) can be shown to be optimal if the error sources (on the background state and on the observations) are assumed to be Gaussian, with known covariances. In the absence of more accurate information, the background error covariance is often modelled using the covariance of system variability (Pham et al., 1998). The Gaussian velocity perturbations in (25) thus represent a reasonable model of the errors that such a classical assimilation scheme can rectify. Two examples of random velocity perturbations $\delta\mathbf{u}$ with the above Probability Density Function (PDF) (26) are illustrated in Fig. 9. In a sequential assimilation scheme, the state variable is updated each time an observation is available. Let us consider that an observation (an ocean tracer image in our case) is available for our reference date k_0 and that the state variable has already been optimally evaluated. We may thus focus exclusively on perturbations of the velocity field $\mathbf{u}_{k_0}$ at this reference date, that is, when this field needs to be corrected by the filtering algorithm. As backward FTLE-V are computed from a time-dependent velocity field, and in order to keep the notations consistent with those used in (14) and (21), we define a perturbed velocity field *sequence* $\mathbf{u}^\lambda = (\mathbf{u}_k^\lambda)_{k=k_0-T}^{k_0}$ by

$$\mathbf{u}_k^\lambda = \begin{cases} \mathbf{u}_k & \text{if} \quad k < k_0, \\ \mathbf{u}_{k_0} + \lambda\delta\mathbf{u} & \text{else}, \end{cases} \tag{27}$$

where $\delta\mathbf{u}$ is a *random* perturbation with PDF (26) and $\lambda \in \Lambda \subset \mathbb{R}$ is a bounded amplitude. A given realization of the random variable (26) is amplified and then applied to the *reference date* velocity field to form a realization of a random perturbed velocity field sequence.

5.2. Results and discussion

In this section we present and discuss the variation of the sensitivity cost function (23) associated with each of the FTLE-V-based DIA triplets

$$\mathcal{E}^\star = (\mathcal{H}_\mathcal{E}, \mathcal{E}, \|\cdot\|_\mathcal{E}), \tag{28}$$

$$\mathcal{V}^\star = (\mathcal{H}_\mathcal{V}, \mathcal{V}, \|\cdot\|_\mathcal{V}), \tag{29}$$

whose elements are defined, respectively, in Sections 4.2 and 4.3. The variation is studied with respect to a bounded amplitude $\lambda \in \Lambda \subset \mathbb{R}$ of the perturbed state $\mathbf{u}^\lambda$ given by (27). Data are provided, respectively, by the corresponding image structure operators (12) and (19) acting on the observed tracer image c at

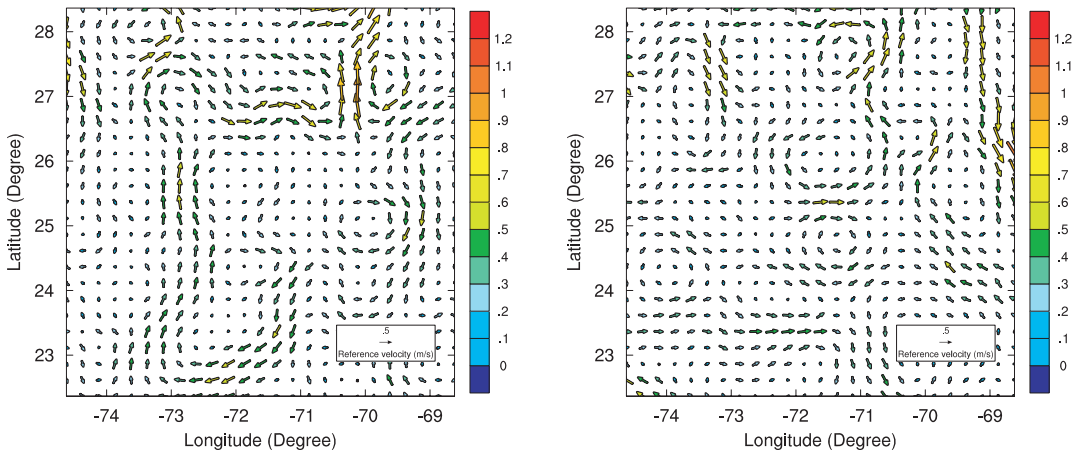

Fig. 9. Example of two random velocity perturbations with the PDF given by (26).

the reference date. We study the particular cases of SST and MLP concentration fields, denoted, respectively, by c_T and c_P. This leads to the definition of the following four sensitivity functions:

$$\tilde{J}^T_{\mathcal{E}}(\lambda) = \|\mathcal{H}_{\mathcal{E}}[\mathbf{u}^\lambda] - \mathrm{E}(c_T)\|^2_{\mathcal{E}}, \tag{30}$$

$$\tilde{J}^T_{\mathcal{V}}(\lambda) = \|\mathcal{H}_{\mathcal{V}}[\mathbf{u}^\lambda] - \mathrm{V}(c_T)\|^2_{\mathcal{V}}, \tag{31}$$

$$\tilde{J}^P_{\mathcal{E}}(\lambda) = \|\mathcal{H}_{\mathcal{E}}[\mathbf{u}^\lambda] - \mathrm{E}(c_P)\|^2_{\mathcal{E}}, \tag{32}$$

$$\tilde{J}^P_{\mathcal{V}}(\lambda) = \|\mathcal{H}_{\mathcal{V}}[\mathbf{u}^\lambda] - \mathrm{V}(c_P)\|^2_{\mathcal{V}}, \tag{33}$$

defined for a given realization of the perturbed state $\mathbf{u}^\lambda$.

Figure 10 shows the variation of the sensitivity functions (30) and (31) corresponding, respectively, to the FTLE-based triplet $\mathcal{E}^\star$ (28) and the FTLV-based triplet $\mathcal{V}^\star$ (29). Results for nine realizations of the random perturbations (27) are plotted with amplitudes in the range $\lambda \in [-4, 4]$. Data come from the corresponding structured observations $\mathrm{E}(c_T)$ and $\mathrm{V}(c_T)$ of the SST fields shown in Fig. 4 (left panel). Figure 11 shows the corresponding results when data come from the MLP concentration field shown in Fig. 4 (right panel). We may first remark that each of the sensitivity functions (30–33) admits a global minimum for the nine random perturbations. Moreover, minima are generally reached around $\lambda = 0$, which corresponds to the non-perturbed state $\mathbf{u}^0$. These two basic aspects clearly show that FTLE-V-based triplets are good candidates for use in ocean tracer image assimilation schemes. More careful examination of these results reveals some important points that merit discussion. First, we may note that each realization of a given sensitivity function exhibits a convex shape around the minimum, which is known to be a good situation for minimization algorithms. From this point of view, the FTLV-based triplet shows smoother variations than the FTLE-based triplet. This is due to the regular behaviour of the

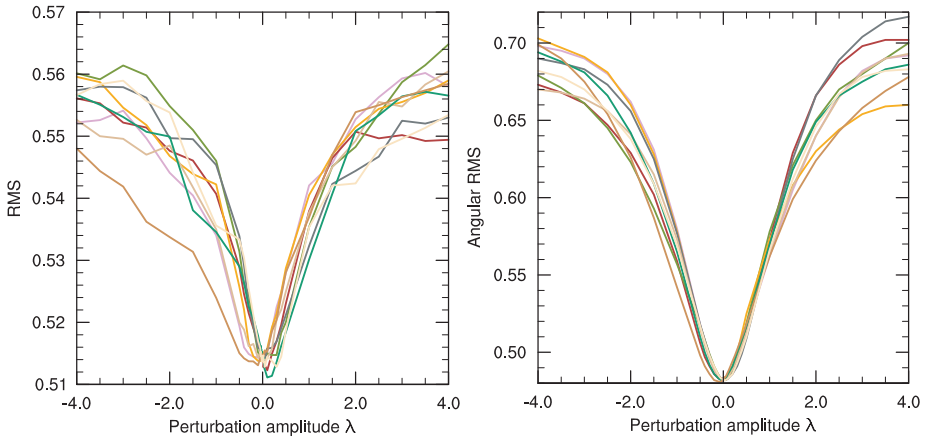

Fig. 10. Behaviour of sensitivity functions for SST. Left: Variation of the sensitivity function $\tilde{J}^T_{\mathcal{E}}$ (30) associated with the FTLE-based triplet $\mathcal{E}^\star$ (28) with respect to the amplitude λ of nine random perturbations (27) applied to the reference velocity field $\mathbf{u}_{k_0}$. Right: Variation of the sensitivity function $\tilde{J}^T_{\mathcal{V}}$ (31) associated with the FTLV-based triplet $\mathcal{V}^\star$ (29) with respect to the amplitude λ of nine random perturbations (27) applied to the reference velocity field $\mathbf{u}_{k_0}$.

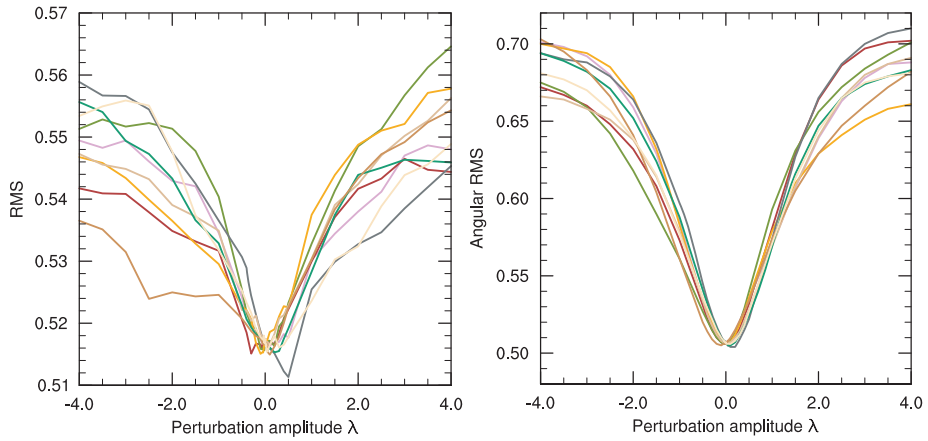

Fig. 11. Behaviour of sensitivity functions for MLP. Left: Variation of the sensitivity function $\tilde{J}^P_{\mathcal{E}}$ (30) associated with the FTLE-based triplet $\mathcal{E}^\star$ (28) with respect to the amplitude λ of nine random perturbations (27) applied to the reference velocity field $\mathbf{u}_{k_0}$. Right: Variation of the sensitivity function $\tilde{J}^P_{\mathcal{V}}$ (33) associated with the FTLV-based triplet $\mathcal{V}^\star$ (29) with respect to the amplitude λ of nine random perturbations (27) applied to the reference velocity field $\mathbf{u}_{k_0}$.

corresponding angular mismatch measure (17). It may thus offer better conditions for the descent-type minimization algorithms widely used in practical applications. One further advantage of the FTLV-based triplet is that it does not depend on any additional 'tuning' parameter like the FTLE-based triplet with the threshold involved in the structure extraction operator (12). Even if the results associated with the FTLE-based triplet depend very little on this parameter—if taken in a reasonable range—this feature should make FTLV-based triplets more robust in practical applications. Secondly, we may observe that the minimum values are not zero. This is not surprising because the Lagrangian tool is known to provide only an incomplete representation of the SST and MLP dynamics. Note, however, that for our application, this is not unsatisfactory. Several reasons can be put forward to explain why FTLE-V structures are not an exact match with the corresponding ones in tracer images for the non-perturbed state. The main reason is probably because ocean tracers such as SST and MLP have their own dynamics that cannot be observed by the Lagrangian tool. The high-resolution tracer gradients also depend on submesoscale dynamics; these dynamics are not taken into account in the computation of FTLE-V because they are computed from a mesoscale field. In addition, FTLE-Vs have been computed at the ocean surface and we know that patterns in ocean colour images (MLP field) are a surface signature of a three-dimensional process. The underlying dynamics also intervene in the formation of these patterns. These aspects, however, are beyond the scope of this paper. Nevertheless, we may note that a zero global minimum value is effectively reached if FTLE-Vs are observed in a precise manner. This is shown in Fig. 12 where sensitivity functions (23) have been computed

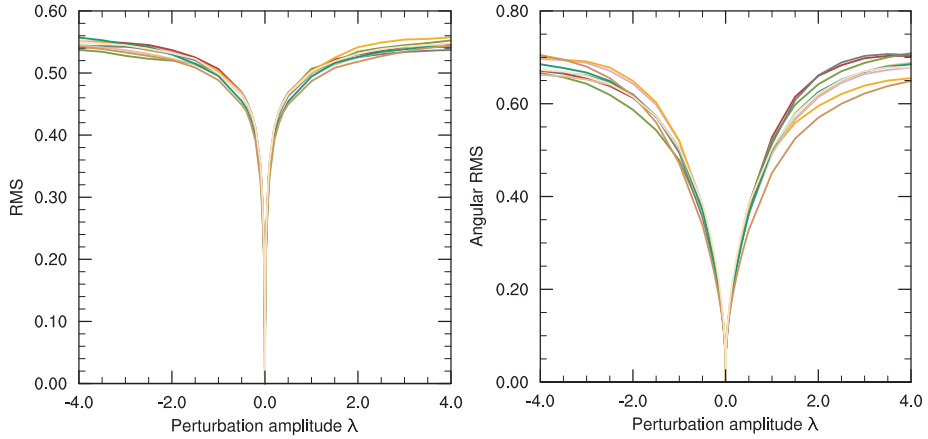

Fig. 12. Variation of the sensitivity function (23) computed with exact model counterpart data $\mathbf{y}^{\mathcal{S}} = \mathcal{H}(\mathbf{X})$. Variation are computed with respect to the amplitude λ of nine random perturbations (27) applied to the reference velocity field $\mathbf{u}_{k_0}$. Left: FTLE-based triplet $\mathcal{E}^\star$ (28). Right: FTLV-based triplet $\mathcal{V}^\star$ (29).

with exact model counterpart data, respectively, $\mathbf{y}^S = \mathcal{H}_\mathcal{E}(\mathbf{u})$ and $\mathbf{y}^S = \mathcal{H}_\mathcal{V}(\mathbf{u})$. Finally, we should point out that some realizations of the sensitivity functions do not reach their minimum at zero (i.e. at the non-perturbed state). This is particularly the case for the FTLE-based triplet, the worse being with MLP data (see Fig. 11, left panel). We also observe the same problem with this tracer for the FTLV-based triplet, but it is less marked. Such behaviour reveals that the data assimilation problem is not well posed in the Hadamard sense, a situation quite common with such inverse problems. To overcome this difficulty, assimilation procedures take into account a priori information about the system that regularize the problem. We should emphasize here that we only studied the image part of the complete data assimilation cost function. We can reasonably expect that the corresponding *full* sensitivity cost-function (which will include a regularization term) will exhibit more regular behaviour.

FTLE-Vs allow us to link mesoscale information from the dynamic part of the model state variable with submesoscale information from the high-resolution tracer fields (images). Our experiments show that, in an idealized case, FTLE-V may be used to directly assimilate high-resolution ocean tracer images into mesoscale eddy-resolving ocean models. An approximate edge detection/location technique used together with the FTLE-based observation operator is sufficient for the sensitivity function to exhibit a minimum value around the reference velocity field, both for SST and MLP concentration images. Observations of gradient orientation show more regular behaviour if used together with the FTLV-based observation operator. Minimization algorithms should be more efficient in this situation.

6. Conclusions

In this paper we have shown that, in an idealized experimental test case, ocean tracer images can be exploited to correct surface model velocities. When viewed as images, SST and MLP fields show relevant features such as eddies, fronts and filaments. Such *structured observations* can be assimilated using a DIA technique. For this purpose we constructed sophisticated observation operators based on FTLE-V computation. These Lagrangian tools are well suited to link *mesoscale* flow dynamics with the *submesoscale* information from ocean tracer images. Lagrangian Coherent Structures represent an elegant alternative to synthetic passive tracer advection in constructing image assimilation observation operators. This kind of operator was used in Titaud et al. (2010) as an example to show the feasibility of direct image assimilation in numerical models. Nevertheless, numerical advection is known to smooth the discontinuities. This feature could be a drawback for image assimilation, but FTLE-V-based operators clearly overcome this problem. The relevance of FTLE-V in a data assimilation framework has been shown using a sensitivity study. Specific objective functions exhibit favourable behaviours for a set of velocity errors. Our perturbation model based on one-year climatological statistics provides a reasonable representation of the errors that common assimilation schemes have to deal with. Even if the FTLE-V structures cannot perfectly match the corresponding structures in the ocean tracer fields under consideration, these results clearly indicate that it is possible to assimilate high-resolution ocean tracer images into mesoscale models using FTLE-V-based observation operators. A more careful examination of the results reveals that FTLV-based observation operators seem more appropriate than FTLE-based one for our application. Nevertheless, a more complete comparison should be conducted to provide a more precise answer to this question. For instance, we may exploit the almost-Lagrangian nature of FLTE (8) to identify the FTLE ridges better. Indeed, it has been shown by Haller (2011) that FTLE gradient and FTLE-V are perpendicular near an FTLE ridge that marks a hyperbolic LCS. Merging FTLE and FTLV properties into a single observation operator may help to constrain the data assimilation system better. As expected in data assimilation, our problem is not well posed (in a mathematical sense), leading to certain defects in some of the realizations of random errors, especially for the FTLE-based operator. This can be overcome (at least partially) by regularizing the minimization problem.

This study is based on synthetic data that were not altered to test the robustness of the method with respect to observation errors, because it is a first step towards the assimilation of ocean tracer images using FTLE-V. Setting up exhaustive experiments to check such robustness is not a straightforward task because observation errors are of different types (measurement error, representativeness errors). For that matter, direct image assimilation is quite unusual with respect to this issue. Indeed, images are spatially structured data (and temporally structured if image sequences are considered), which makes correlations of observation errors hard to model. Furthermore, even though they are crucial questions, they are beyond the scope of this paper and should therefore be the subject of future research.

Finally, we found FTLE-V well suited to satellite image assimilation and the results obtained were very promising. We believe the work presented here also enhances the value of satellite-image products, which are becoming increasingly numerous, with improvements in coverage, frequency and resolution.

7. Acknowledgments

We would like to thank Marina Lévy who provided us with high-resolution bio-dynamical GYRE simulation results of the idealized North Atlantic basin. This simulation has been produced with the support of the Earth Simulator Center, Yokohama Institute for Earth Sciences, JAMSTEC, Japan. We also thank Francesco d'Ovidio who provided us with the code lamta0.3 for computing FTLE-Vs. This work is part of the ADDISA project (reference ANR-06-MDCA-001) supported by the Agence

Nationale de la Recherche (French National Research Agency). Conducting this research would also not have been possible without the continued support of the CNES (French Space Agency). The first author would also like to thank the RTRA STAE scientific foundation for its support in this work. We thank anonymous reviewers for their pertinent suggestions.

The first author dedicates this paper to Alain Largillier.

References

Abraham, E. R. and Bowen, M. M. 2002. Chaotic stirring by a mesoscale surface-ocean flow. *Chaos* **12**(2), 373–381. doi:10.1063/1.1481615.

Artale, V., Boffetta, G., Celani, A., Cencini, M. and Vulpiani, A. 1997. Dispersion of passive tracers in closed basins: beyond the diffusion coefficient. *Phys. Fluids* **9**(11), 3162–3171. doi:10.1063/1.869433.

Aubert, G. and Kornprobst, P. 2006. Mathematical problems in image processing. In: *Applied Mathematical Sciences*, 2nd Edition, Volume 147 (eds. Aubert, G. and Kornprobst, P.). Springer, New York.

Aurell, E., Boffetta, G., Crisanti, A., Paladin, G. and Vulpiani, A. 1997. Predictability in the large: an extension of the concept of lyapunov exponent. *J. Phys. A: Math. Gen.* **30**(1), 1–26. doi:10.1088/0305-4470/30/1/003.

Beron-Vera, F. J. 2010. Mixing by low- and high-resolution surface geostrophic currents. *J. Geophys. Res.* **115**(C10027). doi:10.1029/2009JC006006.

Beron-Vera, F. J. and Olascoaga, M. J. 2009. An assessment of the importance of chaotic stirring and turbulent mixing on the West Florida shelf. *J. Phys. Oceanogr.* **39**(7), 1743–1755. doi:10.1175/2009JPO4046.1.

Beron-Vera, F. J., Brown, M. G., Olascoaga, M. J., Rypina, I. I., Koçak, H., and co-authors. 2008. Zonal jets as transport barriers in planetary atmospheres. *J. Atmos. Sci.* **65**(10), 3316–3326. doi:10.1175/2008JAS2579.1.

Beron-Vera, F. J., Olascoaga, M. J. and Goni, G. J. 2010. Surface ocean mixing inferred from different multisatellite altimetry measurements. *J. Phys. Oceanogr.* **40**(11), 2466–2480. doi:10.1175/2010JPO4458.1.

Brasseur, P. and Verron, J. 2006. The seek filter method for data assimilation in oceanography: a synthesis. *Ocean Dyn.* **56**(5-5), 650–661. doi:10.1007/s10236-006-0080-3.

Carme, S., Pham, D.-T. and Verron, J. 2001. Improving the singular evolutive extended Kalman filter for strongly nonlinear models for use in ocean data assimilation. *Inverse Probl.* **17**(5), 1535–1559. doi:10.1088/0266-5611/17/5/319.

Carmillet, V., Brankart, J.-M., Brasseur, P., Drange, H., Evensen, G. and co-authors. 2001. A singular evolutive extended Kalman filter to assimilate ocean color data in a coupled physical-biochemical model of the north atlantic. *Ocean Model.* **3**, 167–192.

Chan, T. F. and Shen, J. 2005. *Image Processing and Analysis*, (eds. Chan, T. F. and Shen, J.). Society for Industrial and Applied Mathematics (SIAM), Philadelphia, PA.

Corpetti, T., Héas, P., Mémin, E. and Papadakis, N. 2009. Pressure image assimilation for atmospheric motion estimation. *Tellus* **61A**, 160–178. doi:10.1111/j.1600-0870.2008.00370.x.

d'Ovidio, F., Fernández, V., Hernández-García, E. and López, C. 2004. Mixing structures in the mediterranean sea from finite-size Lyapunov exponents. *Geophys. Res. Lett.* **31**(L17203). doi:10.1029/2004GL020328.

d'Ovidio, F., Isern-Fontanet, J., López, C., Hernández-García, E. and García-Ladona, E. 2009a. Comparison between Eulerian diagnostics and finite-size Lyapunov exponents computed from altimetry in the Algerian basin. *Deep-Sea Res.* **51**(1), 15–31. doi:10.1016/j.dsr.2008.07.014.

d'Ovidio, F., Taillandier, V., Taupier-Letage, I. and Mortier, L. 2009b. Lagrangian validation of the mediterranean mean dynamic topography by extraction of tracer frontal structures. *Mercator Ocean Quarterly Newsletter* **32**, 24–32.

Gregg, W. W. 2008. Assimilation of seawifs ocean chlorophyll data into a three-dimensional global ocean model. *J. Mar. Syst.* **69**, 205–225.

Haller, G. 2001a. Distinguished material surfaces and coherent structures in three-dimensional fluid flows. *Physica D* **149**(4), 248–277. doi:10.1016/S0167-2789(00)00199-8.

Haller, G. 2001b. Lagrangian structures and the rate of strain in a partition of two-dimensional turbulence. *Phys. Fluids* **13**(11), 3365–3385. doi:10.1063/1.1403336.

Haller, G. 2002. Lagrangian coherent structures from approximate velocity data. *Phys. Fluids* **14**(6), 1851–1861. doi:10.1063/1.1477449.

Haller, G. 2011. A variational theory of hyperbolic Lagrangian coherent structures. *Physica D: Nonlinear Phenomena* **240**(7), 574–598. doi:10.1016/j.physd.2010.11.010.

Haller, G. and Yuan, G. 2000. Lagrangian coherent structures and mixing in two-dimensional turbulence. *Physica D: Nonlinear Phenomena* **147**(3-4), 352–370. doi:10.1016/S0167-2789(00)00142-1.

Herlin, I., Le Dimet, F.-X., Huot, E. and Berroir, J.-P. 2004. Coupling models and data: which possibilities for remotely-sensed images. In: *e-Environment: Progress and Challenge of Research on Computing Science*, (eds. P. Prastacos, U. Cortés, J.-L. D. D. León and M. Murillo, Vol. 11, Instituto Politécnico Nacional, Mexico, pp. 365–383.

Horn, B. K. P. and Schunck, B. G. 1981. Determining optical flow. *AI* **17**, 185–203.

Krémeur, A.-S., Lévy, M., Aumont, O. and Reverdin, G. 2009. Impact of the subtropical mode water biogeochemical properties on primary production in the North Atlantic: new insights from an idealized model study. *J. Geophys. Res.* **114**(C07019). doi:10.1029/2008JC005161.

Lapeyre, G. 2002. Characterization of finite-time Lyapunov exponents and vectors in two-dimensional turbulence. *Chaos* **12**(3), 688–698. doi:10.1063/1.1499395.

Le Dimet, F.-X. and Talagrand, O. 1986. Variational algorithms for analysis and assimilation of meteorological observations: theoretical aspects. *Tellus* **38A**, 97–110.

Lehahn, Y., d'Ovidio, F., Lévy, M. and Heifetz, E. 2007. Stirring of the northeast atlantic spring bloom: a Lagrangian analysis based on multisatellite data. *J. Geophys. Res.* **112**(C08005). doi:10.1029/2006JC003927.

Lekien, F., Coulliette, C., Mariano, A. J., Ryan, E. H., Shay, L. K. and co-authors. 2005. Pollution release tied to invariant manifolds: a case study for the coast of Florida. *Physica D: Nonlinear Phenomena* **210**(1-2), 1–20. doi:10.1016/j.physd.2005.06.023.

Lévy, M., Estubier, A. and Madec, G. 2001. Choice of an advection scheme for biogeochemical models. *Geophys. Res. Lett.* **28**, 3725–3728.

Lévy, M., Iovino, D., Masson, S., Madec, G., Klein, P. and co-authors. 2009. Remote impacts of sub-mesoscale dynamics on new production. *Mercator Ocean Quarterly Newsletter* **13**, 13–17.

Lévy, M., Klein, P., Tréguier, A.-M., Iovino, D., Madec, G. and co-authors. 2010. Modifications of gyre circulation by sub-mesoscale physics. *Ocean Modelling* **34**, 1–15. doi:10.1016/j.ocemod.2010.04.001.

Luong, B., Blum, J. and Verron, J. 1998. A variational method for the resolution of a data assimilation problem in oceanography. *Inverse Probl.* **14**(4), 979–997. doi:10.1088/0266-5611/14/4/014.

Madec, G. 2008. Nemo ocean engine, In: *Note du Pole de modélisation 27*, Institut Pierre-Simon Laplace (IPSL), Paris, France.

Marr, D. 1982. Vision: a computational investigation into the human representation and processing of visual information. In: *Vision: A Computational Investigation into the Human Representation and Processing of Visual Information*,(ed. Marr, D.). Henry Holt and Co. Inc., New York, NY, USA.

Mathur, M., Haller, G., Peacock, T., Ruppert-Felsot, J. E. and Swinney, H. L. 2007. Uncovering the Lagrangian skeleton of turbulence. *Phys. Rev. Lett.* **98**(14), 144502. doi:10.1103/PhysRevLett.98.144502.

Olascoaga, M. J. 2010. Isolation on the west Florida shelf with implications for red tides and pollutant dispersal in the Gulf of Mexico. *Nonlinear Process. Geophys.* **17**(6), 685–696. doi:10.5194/npg-17-685-2010.

Olascoaga, M. J., Beron-Vera, F. J., Brand, L. E. and Koçak, H. 2008. Tracing the early development of harmful algal blooms on the West Florida shelf with the aid of Lagrangian coherent structures. *J. Geophys. Res.* **113**(C12014). doi:10.1029/2007JC004533.

Olascoaga, M. J., Rypina, I. I., Brown, M. G., Beron-Vera, F. J., Koçak, H. and co-authors. 2006. Persistent transport barrier on the West Florida shelf. *Geophys. Res. Lett.* **33**(L22603). doi:10.1029/2006GL027800.

Ott, E. 1993. *Chaos in Dynamical Systems*, (ed.Ott, E.). Cambridge University Press, New York, USA.

Ottino, J. 1989. *The Kinematics of Mixing: Stretching, Chaos, and Transport*, (ed. Ottino, J.). Cambridge University Press, Cambridge.

Peacock, T. and Dabiri, J. 2010. Introduction to focus issue: Lagrangian coherent structures. *Chaos* **20**(1), 017501. doi:10.1063/1.3278173.

Pham, D., Verron, J. and Roubaud, M. 1998. Singular evolutive extended Kalman filter with EOF initialization for data assimilation in oceanography. *J. Mar. Syst.* **16**(3-4), 323–340.

Pierrehumbert, R. and Yang, H. 1993. Global chaotic mixing on isentropic surfaces. *J. Atmos. Sci.* **50**(15), 2462–2480. doi:10.1175/1520-0469(1993)050<2462:GCMOIS>2.0.CO;2.

Shadden, S. C., Lekien, F. and Marsden, J. E. 2005. Definition and properties of Lagrangian coherent structures from finite-time Lyapunov exponents in two-dimensional aperiodic flows. *Physica D: Nonlinear Phenomena* **212**(3-4), 271–304. doi:10.1016/j.physd.2005.10.007.

Shadden, S. C., Lekien, F., Paduan, J. D., Chavez, F. P. and Marsden, J. E. 2009. The correlation between surface drifters and coherent structures based on high-frequency radar data in Monterey Bay. *Deep-Sea Res.* **56**(3-5), 161–172. doi:10.1016/j.dsr2.2008.08.008.

Titaud, O., Vidard, A., Souopgui, I. and Le Dimet, F.-X. 2010. Assimilation of image sequences in numerical models. *Tellus* **62A**, 30–47. doi:10.1111/j.1600-0870.2009.00416.x.

Wiggins, S. 1992. Chaotic transport in dynamical systems, In: *Interdisciplinary Applied Mathematics*, Volume 2 (ed. Wiggins, S.). Springer-Verlag, Berlin.